ChemPhysChem

Research Article
doi.org/10.1002/cphc.202300231

Chemistry Europe
European Chemical Societies Publishing

www.chemphyschem.org

Special Collection

Structural and Chemical Properties of NiO_x Thin Films: Oxygen Vacancy Formation in O_2 Atmosphere

Raoul Blume,*[a] Wolfram Calvet,[b] Aliakbar Ghafari,[a] Thomas Mayer,[c] Axel Knop-Gericke,[a] and Robert Schlögl[d]

NiO_x films on Si(111) were put in contact with oxygen at elevated temperatures. During heating and cooling in oxygen atmosphere Near Ambient Pressure (NAP)-XPS and -XAS and work function (WF) measurements reveal the creation and replenishing of oxygen vacancies in dependence of temperature. Oxygen vacancies manifest themselves as a distinct O1s feature at 528.9 eV on the low binding energy side of the main NiO peak as well as by a distinct deviation of the $Ni2p_{3/2}$ spectral features from the typical NiO spectra. DFT calculations reveal that the presence of oxygen vacancies leads to a charge redistribution and altered bond lengths of the atoms surrounding the vacancies causing the observed spectral changes. Furthermore, we observed that a broadening of the lowest energy peak in the O K-edge spectra can be attributed to oxygen vacancies. In the presence of oxygen vacancies, the WF is lowered by 0.1 eV.

Introduction

Since the climate change inexorably goes on, the future power supply needs to be further decarbonized. Based on sustainable energies with zero emission of greenhouse gases such as carbon dioxides, this can be realized to some extend by regeneratively produced hydrogen as part of an overall strategy. The advantage of hydrogen is based on the fact that it is storable and can be either used to generate heat by direct combustion or electrical energy in fuel cells. Hydrogen is produced through water splitting in an electrochemical device in which hydrogen and oxygen are generated on the cathode (reduction) and the anode (oxidation), respectively. Hence, this process consists of two half reactions such that the overall efficiency is determined by the half-cell with the slowest reaction rate or kinetics. Thus, it is important to optimize both, the hydrogen evolution reaction (HER) as well as the oxygen evolution reaction (OER) with particular intention on the OER as the generally slower reaction.[1]

Among various 3d-transition metal oxides used as anode material for the OER in alkaline electrolytes, nickel-based oxides are promising candidates. This material presents itself not only as a versatile material in various applications, e.g., in the catalytic oxidation of CH_4 and C_3H_8,[2,3] but also as advantageous with respect to cost, availability, reactivity and the efficiency of the overall electrolytic process in electrochemistry. However, the detailed mechanism underlying the electrochemically induced reaction that in general follows the equation $6\,H_2O \rightarrow O_2 + 4\,H_3O^+ + 4\,e^-$ with a four-electron charge transfer at the liquid solid interface is not yet fully understood. Additional side reactions involving Ni and O species which could lead to additional intermediate phases, mass transport issues or even dissolution or structural transformation processes in the interface region of the catalyst including the sub-surface may complicate the scientific case.[4] The catalytic performance of nickel oxide strongly depends on structural and chemical properties which, in turn, influence the electronic structure such as band structure, density of states (DOS) and conductivity. For example, it has been shown that the efficiency of water splitting on nickel oxide single crystals is affected by the crystal's surface orientation.[5,6,7,8] Moreover, defects, phase boundaries, kinks, and step-edges on the surface can act as reaction centers and even improve the efficiency for water splitting.[7,9,10,11] Hence, since such surface perturbations are usually present on polycrystalline surfaces, it is more accurate to refer to NiO as NiO_x. Furthermore, the importance of porosity and grain size of NiO_x related thin films has been discussed regarding the electrochemical efficiency.[12] It is generally assumed that the catalytically active phase changes according to $NiO \rightarrow Ni(OH)_2 \leftrightarrow NiOOH$ during electrochemical cycling in the anodic potential range. It was recently shown that Nickel oxide when prepared

[a] Dr. R. Blume, Dr. A. Ghafari, Dr. A. Knop-Gericke
Max-Planck-Institut für Chemische Energiekonversion
Postfach 101365, 45413 Mülheim an der Ruhr (Germany)
E-mail: raoul@fhi-berlin.mpg.de

[b] Dr. W. Calvet
Fachbereich 1
Umweltbundesamt
Wörlitzer Platz 1, 06844 Dessau-Roßlar (Germany)

[c] Dr. T. Mayer
FG Oberflächenforschung
TU Darmstadt
Otto-Berndt-Str. 3, 64287 Darmstadt (Germany)

[d] Prof. Dr. R. Schlögl
Abt. Anorganische Chemie
Fritz-Haber-Institut der MPG
Faradayweg 4–6, 14195 Berlin (Germany)

Supporting information for this article is available on the WWW under https://doi.org/10.1002/cphc.202300231

Special Collection An invited contribution to a Special Collection on Synchrotron-Based Photo- and Physical Chemistry

under water atmosphere can form a NiO and $Ni(OH)_2$ based composite with an unclear structure and stoichiometry, hence abbreviated by $NiO_x(OH)_y$, which, compared to NiO_x as starting point, can improve the electrochemical activity.[13] Also, it was shown that $NiO_x(OH)_y$ forms from defective NiO_x when operating the OER reaction.[14] As such, defects in the form of oxygen or Ni vacancies may play a major role in the increase of the observed activity and thus may be crucial for the understanding of the underlying mechanisms of the transformation between the three phases NiO_x, $Ni(OH)_2$, NiOOH and their possible intermediates.

In this paper, as part one of three, results of the interaction of NiO_x with O_2 in dependence of the sample temperature obtained by in situ real-time Near Ambient Pressure X-Ray Photoelectron Spectroscopy, X-Ray Absorption Spectroscopy (NAP-XPS and NAP-XAS, respectively) and work function (WF) measurements as well as DFT-based calculations are discussed. Since NiO_x easily decomposes above 250 °C, NiO_x films were heated in O_2 atmosphere to avoid complete reduction. The obtained high-resolution spectra enable us to determine the requirements for oxygen and Ni vacancy formation, examine their stability and characterize the effect of their presence on the NiO_x electronic structure during the interaction with O_2. This is a pre-requisite for the interaction with gaseous H_2O which will be discussed in a separate work as part two of our studies and, finally, serves also as a starting point of unravelling some details of the OER, which we will present in a third study.

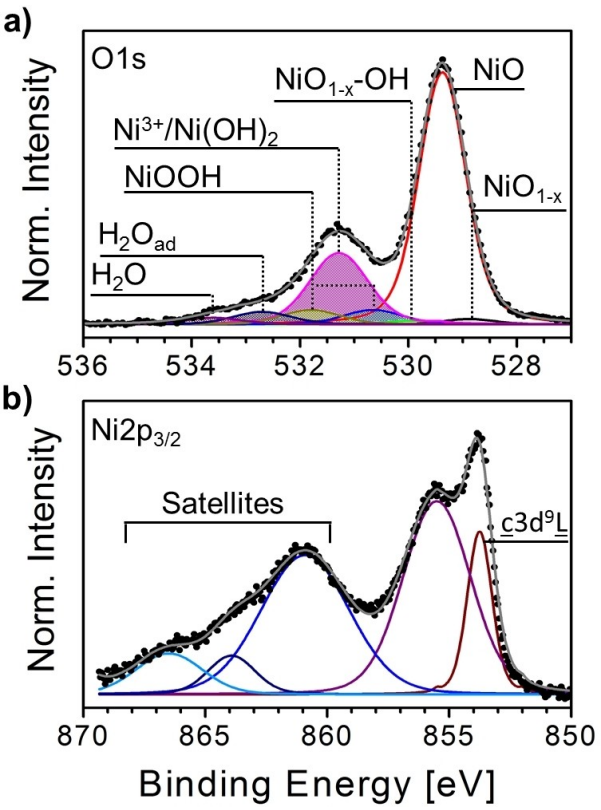

Figure 1. a) XPS spectrum of the O1s region (hν = 880 eV) after oxidation at 250 °C in 0.5 mbar oxygen pressure. Different O1s oxygen species are indicated. b) $Ni2p_{3/2}$ region (hν = 1000 eV) corresponding to a). Both spectra were obtained after evacuation and cooling to RT. The spectra were fitted according to SI-Table 1.

Results and Discussion

Characterization of NiO_x

A 50 nm thick sputtered NiO_x film on n-Si(111) was introduced into the NAP-XPS system and heated stepwise up to 325 °C in vacuum in order to remove native oxides and other contaminants such as carbon that have been formed under atmospheric conditions during transport in air. The resulting metallic Ni film was subsequently oxidised by ramping the sample temperature stepwise from room temperature (RT) to ≈250 °C under an oxygen partial pressure of 0.5 mbar. The transition from metal to oxide takes place between 190 °C and 240 °C within ≈20 min (SI-Figure 2). A Ni film oxidized under such conditions is usually mainly (200) oriented with some contributions of (111) and (110) orientations, which, in our case, results in a predominately flat surface with some rougher patches scattered in between.[15,16,17] A corresponding SEM micrograph is displayed in SI-Figure 3 a).

For comparison with other works characteristic, de-convoluted O1s and $Ni2p_{3/2}$ XPS spectra recorded directly after oxidation at RT in vacuum are displayed in Figure 1 a) and b). Note that always the same colour code is used throughout the following. In the O1s region the dominant feature, attributed to NiO, is located at 529.4 eV.[14,18] Besides this dominating peak, the O1s spectrum also provides a number of additional peaks. The most prominent one is located at about 531.2 eV and is assigned to Ni vacancies, which is considered by some as Ni-deficient NiO or"Ni_2O_3", as we will refer to in the figures.[14,18,19,20,21] To simplify matters, we will use these designations synonymously in the following. Note, that the binding energy (BE) of this peak is very close to the one assigned to $Ni(OH)_2$ and that its presence is one of the reasons to refer to Ni oxide as NiO_x.[22,23] Two other peaks at 530.65 eV and 531.9 eV, respectively, can be assigned to NiOOH reflecting the two oxygen atoms in different electronic configurations.[14,21,24] Furthermore, peaks related to single and multi-layer H_2O adsorption are found on the high binding energy side of the spectrum.[14,21] The two very weak components at 528.9 eV and 530 eV, indicated as NiO_{1-x} and NiO_{1-x}–OH, respectively, will be addressed in detail later on. The fit of the $Ni2p_{3/2}$ spectrum shows a series of peaks and satellites as a result of the photoemission process. As Ni is a transition metal the $Ni2p_{3/2}$ spectra are dominated by final state effects which leads to a complex electronic structure which is partially still under discussion. The NiO main line at 853.7 eV is commonly assigned to a $\underline{c}3d^9\underline{L}$ final state configuration ($\underline{L}$: ligand hole; $\underline{c}$: core hole) while the extended satellite region above 860 eV is attributed to $\underline{c}3d^{10}\underline{L}^2$ and $\underline{c}3d^8$ final states.[25,26] In contrast, the origin of the shoulder at the high binding energy side of the main peak is more difficult to explain. While it is often simply attributed to Ni^{3+} or "Ni_2O_3" formed due to Ni vacancies in the NiO lattice, it may stem from multiplet splitting or non-local screening effects

as well.[19,26,27,28] Recently, combined experimental and theoretical studies of NiO showed that also surface related effects such as island nucleation or sputter-induced defects contribute to this peak.[29,30,31,32] With respect to the results that are presented in this work, all of these aspects need to be considered and will be addressed below. A detailed description of the fit model including its complex satellite structure based on the work of Biesinger et al. is given in the Supporting Information.[33,34]

Heating of NiO_x in Oxygen

In order to investigate the thermal stability of the NiO_x surface, a fresh NiO_x film was heated up to 650 °C in 0.5 mbar O_2. The full set of $Ni2p_{3/2}$, O1s and VB spectra is shown in SI-Figure 4. Spectra of the $Ni2p_{3/2}$ and the O1s regions recorded at 20 °C in vacuum before heating and at the maximum temperature of 650 °C are depicted in Figures 2a) and b), respectively, showing distinct variations of the NiO_x spectra at different temperatures. In particular, the characteristic $Ni2p_{3/2}$ main spectral feature with its stepped doublet structure indicating NiO becomes flatter at high temperatures (Figure 2a). The intensity change centres mostly around 855 eV. Upon cooling, the typical NiO_x double peak structure is regained (SI-Figure 4a). Interestingly, changes observed in the VB region appear very similar to what is observed in the $Ni2p_{3/2}$ region (SI-Figure 4c). The alterations observed in the corresponding O1s spectra behave differently as depicted in Figure 2b). With increasing temperature, the main O1s feature broadens while the secondary intensities at high BEs, which are related to Ni-deficient NiO, decrease. After cooling at the end of the experiment the original intensity of this feature is clearly not reached again (SI-Figure 4b).

By making use of multi-peak fit routines based on the peaks listed in SI-Table 1, the fits of the $Ni2p_{3/2}$ and O1s spectra reveal further details on changes of the NiO_x film during the heating to 650 °C in O_2. Figure 2d), bottom panel, depicts the O1s fits of the spectrum recorded at $T_{max} = 20$ °C in vacuum. Compared to its 650 °C counterpart (top panel) it clearly shows the presence of the Ni^{3+}-related peak at 531.2 eV with almost half of the intensity of the main oxide peak at 529.4 eV. At 650 °C the former peak has vanished while the main oxide peak is flanked by two peaks at 528.9 and 530 eV, labelled as NiO_{1-x} and NiO_{1-x}–OH, respectively. The corresponding $Ni2p_{3/2}$ spectra in Figure 2c) show that a fit with oxide peaks alone leaves a residuum, which, even with slight changes of the intensities of the fitted components, cannot be compensated. A detailed overview of the evolution of the Ni-to-oxygen ratio, the $Ni2p_{3/2}$ residuum and the O1s fits is given in Figures 3a) to c). During heating to 650 °C, several strong trends are observed. Firstly, the O1s peak at ≈531.2 eV attributed to Ni-deficient NiO is continuously decreasing throughout the whole experiment. Even after cooling at the end of the experiment, the original intensity of the Ni-deficient NiO is clearly not reached again. Simultaneously, the $Ni2p_{3/2}$ residuum continually increases up to ≈400 °C. Remarkably, only after cooling it appears to decrease again such that its corresponding $Ni2p_{3/2}$ spectrum is virtually identical to the one prior to heating. This behavior suggests that the observed dynamics of the $Ni2p_{3/2}$ spectra are not related to Ni^{3+}. Secondly, starting just above 350 °C the relative intensities of the peaks labelled NiO_{1-x} at 528.9 eV and NiO_{1-x}OH at 530 eV increase. The relative intensity of the former becomes higher than that of the latter reaching relative maxima of about 0.22 and 0.1 at about 500 °C, respectively. This apparent saturation is reflected by the behaviour of the $Ni2p_{3/2}$ residuum, which also reaches a maximum level at around the same temperature. However, in the end, after cooling, both, the intensities of the NiO_{1-x} and the NiO_{1-x}OH peak are almost completely quenched. In addition, while the $Ni2p_{3/2}$ is back to the typical NiO shape, the O1s spectrum has still significantly changed due to the almost complete loss of the intensity of the

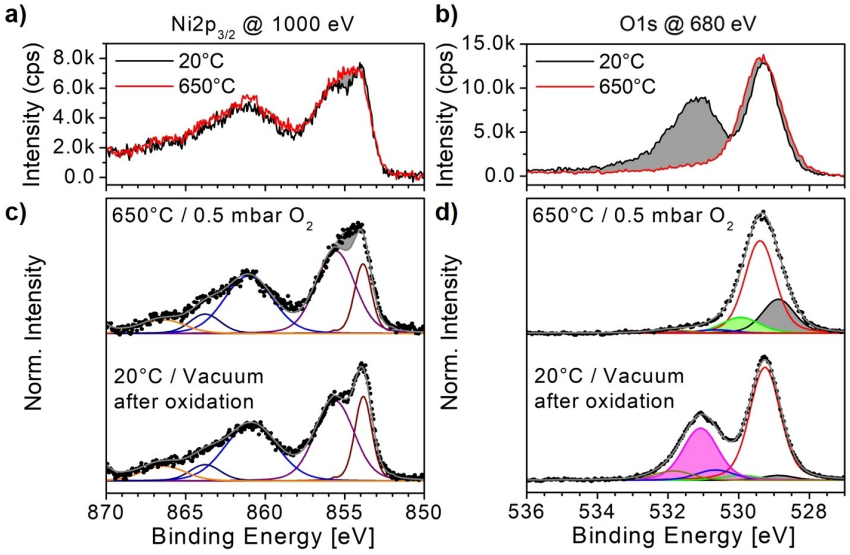

Figure 2. NiO_x film heated at 0.5 mbar O_2 atmosphere. a) and b) Direct comparison of $Ni2p_{3/2}$ and O1s spectra recorded at RT prior to heating and at 650 °C. c) $Ni2p_{3/2}$ spectra of a) fitted with NiO components only. d) O1s fits of b). To highlight their strong intensity variations, the peaks at 531.2, 528.9 and 530 eV are filled with different colors. The spectra were fitted according to SI-Table 1.

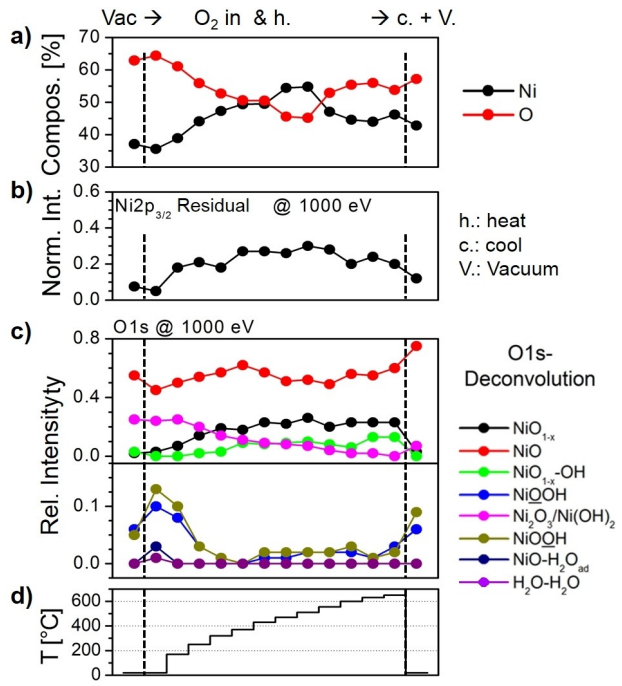

Figure 3. a) Evolution of the Ni and O fractions during heating to 650 °C. b) Evolution of the residual intensity derived from subtracting the pure NiO fit from the measured Ni2p$_{3/2}$ spectrum (grey areas in Figure 2a) and c) with temperature. c) Evolution of the relative intensities derived from the fits of O1s spectra with temperature. The spectra were fitted according to SI-Table 1. Note that the photon energies for the O1s and Ni2p$_{3/2}$ spectra represent the same information depth. d) Heating profile.

531.2 eV peak. Thirdly, changes in composition of Ni and O suggest a stronger loss of oxygen reaching a maximum at ≈500 °C (Figure 3a). Interestingly, beyond this temperature the sample appears to gain oxygen again. This is somewhat counter intuitive because of the high temperature of the sample. The reason for the oxygen increase partially lies in the increase of the peak labelled NiO$_{1-x}$–OH, which we will briefly address below, as well as in the formation of small amounts of NiOOH (Figure 3c), bottom panel). Together with the simultaneous decrease of Ni vacancies represented by the peak at 531.2 eV, they account for most of the oxygen increase above 550 °C.

The relation between the Ni2p$_{3/2}$ intensity variations with the peaks at 528.9 and the 530 eV peak (labelled Ni$_{1-x}$ and NiO$_{1-x}$–OH) as well as the peak related to Ni-deficient NiO at 531.2 eV, was further investigated by heating a freshly prepared NiO$_x$ film three times up to only ≈350 °C in 0.5 mbar O_2. The full set of O1s and Ni2p$_{3/2}$ spectra is shown in SI-Figure 5. Spectra of the O1s and the Ni2p$_{3/2}$ regions recorded at the temperature maximum at 350 °C and after subsequent cooling to 150 °C are depicted in Figures 4a) and b), respectively. The alterations observed in the O1s spectra depicted in Figure 4a) behave similar but not exactly the same as by heating to 650 °C. At T_{max} = 350 °C the main O1s feature broadens again while the secondary intensities at high BEs which may be related to Ni-deficient NiO decrease. However, this time the latter is not completely quenched and both features revert to their original state upon cooling to 150 °C. In the corresponding Ni2p$_{3/2}$ region the distinct flattening of characteristic main spectral feature with its stepped doublet structure at high temperatures can be observed again (Figure 4b). The intensity changes centre mostly around 855 eV but also a small difference between the second and third peak at ≈858 eV in the spectrum is found. Upon cooling the typical NiO$_x$ double peak structure is regained. These changes are, again, also reflected in the VB region, which appears very similar to what is observed in the Ni2p$_{3/2}$ region (see below, Figure 7d).

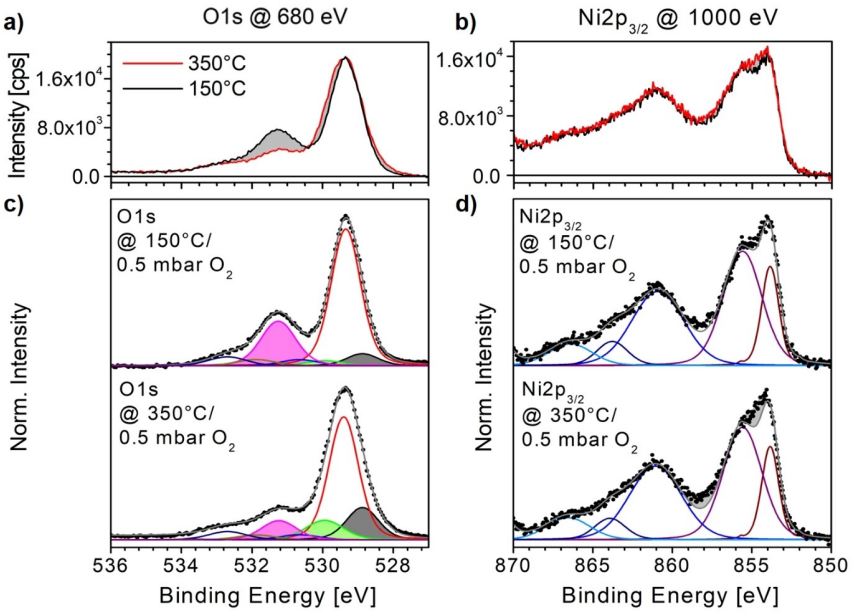

Figure 4. NiO$_x$ film heated at 0.5 mbar O_2 atmosphere. a) O1s spectra recorded at T_{max} = 350 °C and after subsequent cooling to 150 °C. b) Ni2p$_{3/2}$ spectra corresponding to a). c) O1s fits of spectra in a). The peaks at 531.2, 528.9 and 530 eV are highlighted. d) Ni2p$_{3/2}$ spectra of a) fitted with NiO components only. The spectra were fitted according to SI-Table 1.

The fits of the Ni2p$_{3/2}$ and O1s spectra were performed by applying the multi-peak fit routines based on the peaks listed in SI-Table 1. Figure 4c), bottom panel, depicts the O1s fits of a spectrum recorded at T_{max} = 350 °C. Compared to its 150 °C counterpart (top panel), it shows a broadening around the main NiO peak due to increasing intensities of the already observed peaks at 528.9 and 530 eV, labelled as NiO_{1-x} and NiO_{1-x}–OH, respectively. Simultaneously, the intensity of the peak attributed to Ni-deficient NiO at 531.2 eV decreases significantly. However, at only 350 °C it does not vanish completely and obviously regains a high intensity after cooling to 150 °C. On the other hand, the differences between the corresponding Ni2p$_{3/2}$ spectra are very similar to what was observed by heating to 650 °C. While the 150 °C spectrum can be satisfactorily fitted with NiO components alone, the spectrum recorded at 350 °C confirms a strong residuum mainly visible at ≈855 eV, marked in grey, when fitted with oxide peaks.

This behaviour of the O1s and Ni2p$_{3/2}$ regions is virtually the same throughout all three heating-cooling cycle indicating a reversible process. More details are revealed by following evolution of the Ni-to-O ratio, the Ni2p$_{3/2}$ residuum and the O1s fits (Figure 5). During the heating-cooling cycles a small but noticeable change of the Ni-to-O ratio is observed (Figure 5a). At higher temperatures the Ni fraction slightly increases while the O fraction decreases. Upon cooling both fractions reverse almost to their original values. However, over the course of three heating-cooling cycles there seems to be a very small overall oxygen uptake. Note, that the higher oxygen fractions at 20 °C and 120 °C which are cut off in Figure 5a) are due to overlapping peaks of adsorbed C–O species which are fully depleted at 230 °C according to the corresponding C1s signal (not shown). As soon as heating in O_2 starts, the relative O1s intensities, depicted in Figure 5c) begin to change. Up to ≈200 °C only moderate changes are observed, which are mainly related to the removal of the residual adsorbed C–O species on the surface. Above 200 °C the contaminant-free composition is reached. Here, a relative intensity decrease of both, the main NiO as well as the peak assigned to Ni-deficient NiO can be seen. Both, the 528.9 and the 530 eV peak (labelled NiO_{1-x} and NiO_{1-x}–OH, respectively), gain intensity simultaneously with the former reaching slightly higher relative intensities of ≈0.13 a little earlier. This behaviour proceeds until the first temperature maximum is reached. Note that the relative intensities of both peaks gained here are lower than the maximum value of 0.22 reached at ≈500 °C in Figure 3c). Upon subsequent cooling, the situation for all relative peak intensities is almost entirely reversed when the O1s NiO main peak and the peak attributed to Ni-deficient NiO at 531.2 eV reach their original values. Interestingly, both, the 528.9 and the 530 eV peak retain some intensity even after cooling, which suggests a change of the sample surface with respect to the freshly prepared oxide film. Almost identical spectral sequences are observed during two further heating-cooling cycles. Compared to these relative intensity changes, the adsorbat- and NiOOH-related intensities vary only scarcely with slight decreases, partially to zero intensity, at high temperatures and similarly small increases upon cooling, pointing to a minor role in the observed picture. The striking relative intensity variations observed in the O1s region coincide with distinct changes observed in the Ni2p$_{3/2}$ region. Figure 5b) follows this by monitoring the evolution of the residuum obtained from subtracting a fitted pure NiO spectrum from the respective measured spectrum in dependence of sample temperature (grey areas in Figure 4d). Apparently, the residuum increases and decreases with temperature following the evolution of the O1s peaks at 528.9 and the 530 eV peaks (labelled NiO_{1-x} and NiO_{1-x}–OH, respectively) except for a thermal delay during cooling after each temperature maximum (T_{max}), while, on the other hand, behaving diametric to the 531.2 eV peak. Furthermore, the normalized maximum intensity of the residuum is just as strong as observed when heating to 650 °C.

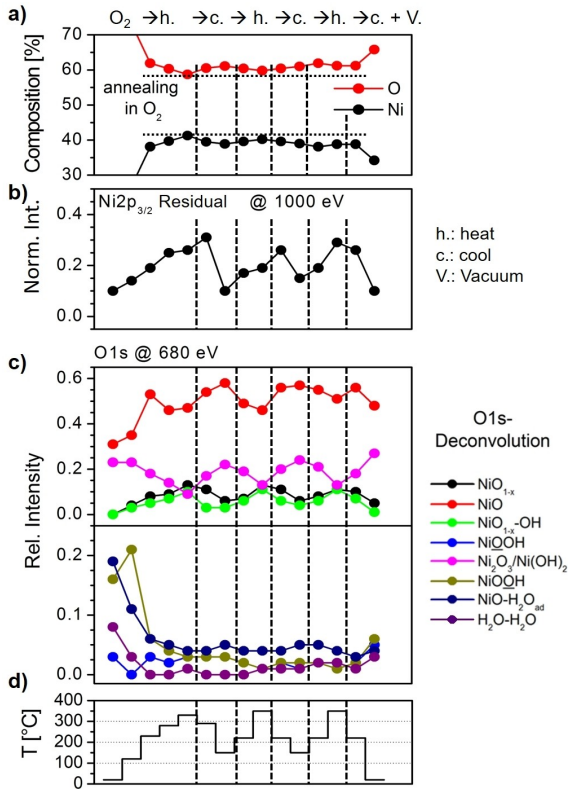

Figure 5. a) Ni and O fractions during several heating-cooling cycles in dependence of the sample temperature. b) Evolution of the Ni2p$_{3/2}$ residuum intensity derived from subtracting the pure NiO fit from the measured spectrum (grey areas in Figures 3b) and d) with temperature. c) Evolution of the relative intensities of oxygen species with temperature as derived from the fits of O1s spectra. The spectra were fitted according to SI-Table 1. Note that the photon energies for the O1s and Ni2p$_{3/2}$ spectra represent the same information depth. d) Heating profile.

XAS Results

The NiO_x samples were also monitored by XAS during the heating-cooling cycles. In Figure 6a) the Ni L_3-edges of the NiO_x sample exposed to 0.5 mbar O_2 are shown at RT before heating, at the third heating maximum at 350 °C as well as at RT after the third heating to 350 °C, respectively. Both spectra recorded at 20 °C are virtually identical and reflect the typical signature of

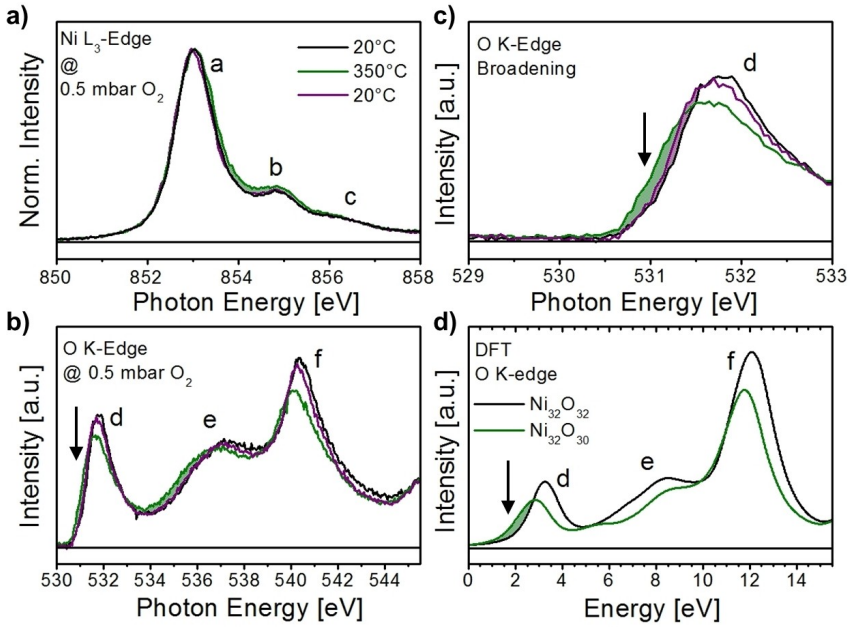

Figure 6. a) XAS spectra of the Ni L_3-edges of the NiO_x sample at 150 °C, at 350 °C and after cooling to 150 °C in 0.5 mbar O_2, respectively. b) XAS spectra of the O K-edges corresponding to a). c) Close-up of feature d in the O K-edge spectra. d) Calculated XAS spectra for NiO without ($Ni_{32}O_{32}$) and with bulk oxygen vacancies ($Ni_{32}O_{30}$). The features a–f are explained and discussed in the text. Note that the intensities in a) are normalized to peak a.

bulk NiO with Ni^{2+} according to multiplet calculations assuming the nickel ion be located in a cubic crystal field environment O_h.[35,36,37,38] The spectra are split into two groups at around 854 eV (L_3) and 872 eV (L_2, not shown here) due to spin-orbit interactions of the $2p^5$ core-levels ($2p^5{}_{3/2}$ and $2p^5{}_{1/2}$) similar to XPS. Features a and b in the Ni-L_3 spectra correspond to Ni^{2+} related $2p^63d^8 \rightarrow 2p^53d^9$ transitions which are dominated by multiplet effects. Feature c is attributed to excitations into $2p^53d^{10}\underline{L}$ final states.[38] At T_{max} both peak structures a and b in the Ni L_3 spectrum exhibit a broadening towards lower photon energies which also leaves the dip between both peaks less pronounced. This behaviour resembles the evolution of the $Ni2p_{3/2}$ spectra recorded at the same temperatures (Figure 4d).

The corresponding O K-edge spectra exhibit even more variations as shown in Figure 6b) (see also SI-Figures 6 and 7). While the spectra recorded at RT appear almost identical similar to the behaviour of their Ni L_3-edge counterparts, a pronounced shift of the peaks labelled e and f as well as a notable broadening of the low energy side of peak d is observed at T_{max} (indicated by an arrow). The latter is shown as a close-up in Figure 6c).

Discussion

Given the similar behaviour of XPS and XAS, the observed changes strongly suggest a common basic cause. Let's first turn our attention to XAS. In combined experimental and theoretical studies about NiO nanoparticles and NiO islands on HOPG, peaks e and f in Figures 6b) and c) were previously assigned to mixed unoccupied O2p–Ni4sp states while peak d was assigned to unoccupied Ni e_g states.[35,36,39] It was shown that missing surface oxygen atoms lead to a broken symmetry causing a split of the unoccupied e_g states into several peaks around 532 eV which manifest themselves by a distinct broadening of feature d. For comparison to our case XAS spectra of a relaxed 2×2×2 supercell consisting of 32 Ni and 32 O atoms and a similar supercell containing only 30 O atoms, i.e., with two bulk vacancies, were calculated (Figure 6d). The simulated $Ni_{32}O_{32}$ spectrum agrees well with our experimental results. With the introduction of oxygen vacancies, peaks e and f exhibit shifts, also in agreement with the experimental data. Furthermore, the $Ni_{32}O_{30}$ spectrum features a distinct broadening of peak d towards low energies (marked by an arrow) which shows that the formation of oxygen vacancies in bulk NiO can lead to a similar situation than found for missing surface oxygen in NiO clusters and islands. In conclusion, the XAS data strongly suggest the presence of oxygen vacancies formed at or in the vicinity of the NiO_x film's surface at high temperatures.

The interpretation of the XPS data is even more complex. The nature of the $Ni2p_{3/2}$ shoulder of the NiO_x main feature between 855 and 856 eV is still under discussion.[19,26,27,28] The intensity gain at about 855 eV during heating of the samples in our experiments may be explained by an increase of Ni^{3+} oxidation states (Ni_2O_3), representing Ni vacancies in the NiO surface, which seems to be plausible under oxygen atmosphere at elevated temperatures. However, regarding the obtained results this explanation does not fit the picture. The O1s related emission corresponding to Ni^{3+} as in Ni_2O_3 or Ni deficient NiO is located at about 531.2 eV which is on the higher binding energy side of the O^{2-} related main peak at 529.4 eV attributed to NiO. When the sample is heated and subsequently cooled, this peak's intensity behaves diametrically to the $Ni2p_{3/2}$ residuum. Hence, the assignment of the intensity change at

≈855 eV to Ni^{3+} is not plausible in the present case. Since, in contrast, the emissions on the low and the high binding energy side of the NiO peak at 528.9 eV and 530 eV, respectively, follow almost exactly the same intensity change pattern as the $Ni2p_{3/2}$ residuum, both O1s and the Ni2p features appear to be related to each other excluding an influence of a Ni^{3+} state.

Recently, combined experimental and theoretical studies focused on the shape and evolution of the emissions from the Ni2p states using depth profiling and thin film NiO_x growth techniques. They revealed that the line intensity at ≈855–856 eV is more pronounced for a higher surface sensitivity as well as for the early stages of the NiO_x film formation in the monolayer regime and also, as simulated by NiO cluster configurations, for oxygen deficiencies.[26,29,30,32] Furthermore, either by preparing NiO nanocrystals or by creating defects through Ar-sputtering similar changes in the Ni2p spectra were observed accompanied by a broadening of the O1s contribution on the low binding energy side of the main NiO peak.[31,40] Rieck et al. also obtained similar spectra for cone-like Ni/NiO micro-structures.[41] They found that at least parts of the $Ni2p_{3/2}$ signal are due to Ni^{3+} because the corresponding O1s emission also shows contributions of NiOOH besides NiO and $Ni(OH)_2$. In addition, a pronounced O1s peak in the binding energy regime below the main O1s line corresponding to NiO was observed. Finally, it was found that two-dimensional amorphous NiO nano-flakes yield somewhat flattened $Ni2p_{3/2}$ spectra and, in parallel, they exhibit strong O1s intensities in the lower binding energy range due to under-coordinated Ni atoms at the rims of the nano-flakes.[42] Based on this background the changes observed in our experimental data are most certainly defect related as well. Normally, heating of NiO in vacuum would lead to a fast reduction of the oxide above temperature of 250 °C as observed, e.g., for the reduction of native oxide during preparation of samples. Hence, under the given conditions, i.e., heating up to T_{max} = 350 °C or even 650 °C in 0.5 mbar O_2 atmosphere, it is feasible that, instead of full reduction, oxygen vacancies are formed manifesting themselves as spectral features in the Ni2p and O1s regions at ≈855 eV and 528.9 eV, respectively. Thus, the latter was labelled NiO_{1-x}. Interestingly, under the applied conditions, the formation of oxygen vacancies seems to be limited as evidenced by the saturation of the relative peak intensity between ≈500 °C and 650 °C displayed in Figure 3c). Since the apparent formation of –OH bonds is obviously also limited, the other potential source of additional oxygen is the gas phase O_2. The dissociation of oxygen molecules must set in already at lower temperatures because in vacuum NiO reduces completely already at ≈350 °C. However, a small oxygen loss is observed up to ≈500 °C when the maximum oxygen vacancy level is reached. It appears, that at this temperature dissociation of O_2 (and, judging by the formation of small NiOOH amounts, also of H_2O from residual gas) becomes effective enough to prevent further reduction at least up to 650 °C. Upon cooling in oxygen, the oxygen vacancies are replenished leading to a decrease of both, the ≈855 eV and 528.9 eV intensity contributions. Note, that after applying the heating-cooling treatment, the morphology of the surface has also changed towards a more terraced surface (SI-Figure 3b). The possible nature of the other newly observed O1s component at 530 eV will be discussed in detail in a second part of our studies of oxygen vacancies on NiO_x which is currently in preparation. However, in short, we assign this peak to oxygen vacancies which chemisorb OH stemming, in the present case, from the dissociation of H_2O out of the residual gas. H_2O dissociation is known to occur favorably at defects or step-edges and requires "non-lattice" oxygen, to form OH which, here, is directly provided by the oxygen atoms removed from the vacancy sites.[8,43,44] Then, at high sample temperatures this OH can chemisorb at oxygen vacancies shifting their apparent binding energy to 530 eV, hence the label NiO_{1-x}–OH. Upon cooling this chemisorbed OH can act as a precursor to subsequent NiOOH formation. Note, that, according to O1s depth profiling the relative intensity changes observed for the NiO_{1-x} and NiO_{1-x}–OH peaks at 528.9 and the 530 eV, respectively, as well as for the peak at 531.2 eV related to Ni-deficient NiO are rather surface related supporting their nature as surface vacancies. A detailed description of the depth profiling is given in SI-Figure 8.

Several other of our observations further corroborate this appearance of oxygen vacancies during heating in O_2 atmosphere. Firstly, density-of-states (DOS) calculations were performed comparing bulk $Ni_{32}O_{32}$ with $Ni_{32}O_{30}$ configurations with two randomly distributed oxygen vacancies (Figure 7e). It should be noted that in these calculations a broadening has been considered in order to compare with the XPS data. The simulations reveal that such vacancies can account for the changed peak intensities observed in the VB region close to the Fermi Edge during heating in oxygen as presented in Figure 7d). This is visible as a small loss of O2p partial DOS and a distinct change of the Ni3d partial DOS similar to what is observed in the $Ni2p_{3/2}$ region as well. However, due to the matrix element, cross section and photon energy the DOS is slightly different to the XPS measurement. Further DFT calculations also explain why an oxygen vacancy manifest itself as a peak on the low binding energy side of the main O1s intensity related to NiO while a Ni vacancy, also labelled as Ni_2O_3 or Ni^{3+}, is observed on the high binding energy side. The relaxed structures, obtained by DFT, are shown as charge density and as schematic bond length plots in Figures 7a)–c), left and right, respectively. They reveal that in comparison with bulk $Ni_{32}O_{32}$ the charge density as well as bond lengths between Ni and O atoms surrounding an oxygen vacancy in $Ni_{32}O_{31}$ and a Ni vacancy in $Ni_{31}O_{32}$ are strongly affected by the presence of the respective vacancy. While in the case of an oxygen vacancy the surrounding Ni atoms relax towards the vacancy, in the case of a Ni vacancy the surrounding oxygen atoms relax outwards. Interestingly, in both cases the charge densities as well as the bond lengths between the nearest neighbouring atoms to the respective vacancy, i.e., the surrounding atoms, remain almost unchanged. Instead, for an oxygen vacancy the charge density between the nearest neighbour Ni and the second nearest neighbour O atoms is decreased (as exemplarily highlighted by the orange oval in Figures 7c) while the bond lengths between these atoms is increasing letting the Ni atoms moving closer together. In

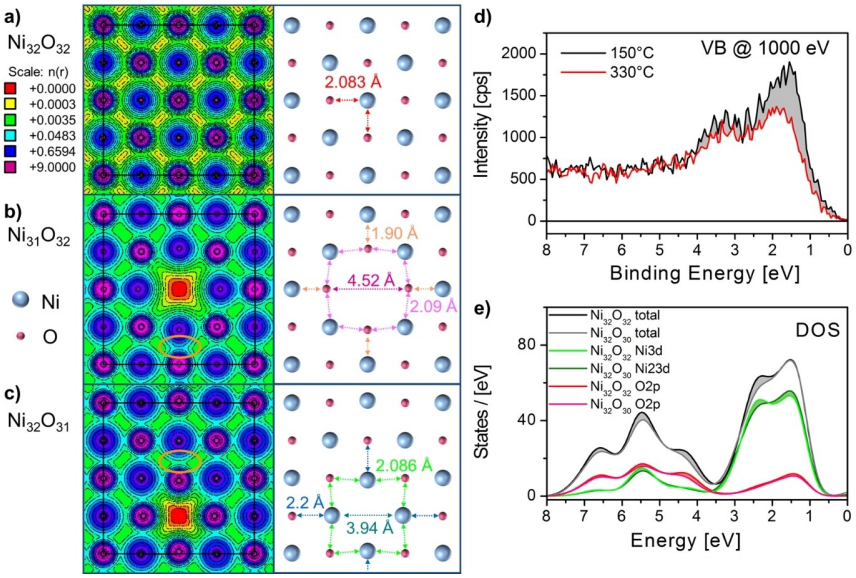

Figure 7. a) to c): Relaxed structures of 2×2×2 unit cells with a) $Ni_{32}O_{32}$, b) $Ni_{31}O_{32}$ with a Ni vacancy and c) $Ni_{32}O_{31}$ with an O vacancy. Differences of charge densities Δn(r) on the left are indicated by colour. Distances between several Ni and O atoms around a vacancy site on the right are indicated by their values and by differently coloured arrows. d) VB spectra recorded subsequently at 330 and 150 °C of the first heating-cooling cycle corresponding to Figure 2 a) and b). e) DOS calculation of bulk $Ni_{32}O_{32}$ and $Ni_{32}O_{30}$. For both, the total DOS as well as the partial DOS of Ni3d and O2p states are displayed in different colors. Notable intensity variations are filled in with grey, green and red, respectively.

consequence, the Ni–O bond strengths around the vacancy are weakened and the oxidation state of the Ni atoms is effectively lowered which leads to the appearance of the low binding energy peak, thus labelled NiO_{1-x}. This is further supported by DFT based calculations of XPS BE, which reveal that by introducing an oxygen vacancy into the crystal the oxygen BE is lowered by 1.4 eV which is in good agreement with the experimental data for which a negative shift of 0.5 eV with respect to the main NiO peak is observed. These observations can also help to understand how NiO reduction is initiated by forming metallic Ni "islands" through successive removal of oxygen atoms. In the opposite case of a Ni-vacancy the charge density between the nearest neighbour O and the second nearest neighbour Ni atoms is increased (again exemplary highlighted by an orange oval in Figure 7 b) while the respective bond lengths are decreased. Thus, the Ni–O bonds around the Ni-vacancy are strengthened leading to a Ni^{3+} oxidation state which accounts for the presence of the O1s peak at 531.2 eV. This also confirms to some extend the interpretation of this peak as Ni_2O_3 seen in the references. Remarkably, the results presented above clearly show that any permanent effect on XPS spectra caused by a changed "chemical" environment is found in the O1s rather than the Ni2p region. As seen in Figure 5 c) after three heating-cooling cycles there are some oxygen vacancies left while the $Ni2p_{3/2}$ spectrum fully reverts to its original shape. Furthermore, while the Ni vacancy related peak at 531.2 eV in the O1s region is so strongly affected by heating to 650 °C that even after subsequent cooling it does not regain its original intensity by far, the $Ni2p_{3/2}$ spectrum is not affected at all (SI-Figure 4). Hence, to address the open question from above, the shoulder on the high BE side of the $Ni2p_{3/2}$ main peak is most likely related to non-local screening effects rather than caused by a chemical shift which would explain the indirect relation between this shoulder and the peaks observed in the O1s region. This needs to be addressed by detailed theoretical studies which is beyond the present work. However, more details on the spectral shapes will be provided in another manuscript as a second part of our studies.

In a further experiment the WF was monitored during oxidation of metallic Ni and subsequent heating-cooling cycles as shown in SI-Figure 9. After full oxidation of Ni to NiO_x at 350 °C and subsequent cooling to 20 °C the WF measured in O_2 atmosphere is 5.0 eV which is in the expected range.[45,46,47] During the following heating-cooling cycles the WF alternates between higher values at low temperatures and lower values at high temperatures. For NiO_x a higher WF is expected in the presence of electronegative species, which, in our case, is provided by Ni vacancies prominently present at RT (see Figures 1 a), 2 d) and 4 c).[48] In contrast, with the vanishing of Ni vacancies and the formation of oxygen vacancies at $T \geq 340$ °C the electronegativity is decreased leading to a decrease of the WF by ≈0.1 eV. This value is significantly smaller than the WF-decrease of 1.4 eV observed during partial reduction of NiO by Greiner et al.[45] However, in the present case the "partial reduction" is limited to the formation oxygen vacancies only leading to smaller WF change. During the heating-cooling cycles a small overall increase of the WF is visible. This may be related to the formation of small amounts of NiOOH (see Figures 3 c) and 5 c) which reportedly increases the WF above the NiO_x value,[49] but it could also stem from further, undetected structural changes.

Conclusions

We have investigated NiO_x thin films in situ under 0.5 mbar oxygen pressure at temperatures ranging from RT to 650 °C using NAP-XPS, NAP-XAS, WF measurements and DFT calculations. Heating and cooling in oxygen reveal the creation and replenishing of oxygen vacancies in dependence of sample temperature. Ni vacancies are only notably present at lower sample temperatures and can even be almost fully eliminated by heating beyond 500 °C. In contrast, a maximum of oxygen vacancy formation is reached at approximately 500 °C at which the formation saturates. The vacancy formation manifests itself as a distinct O1s feature at 528.9 eV, labelled NiO_{1-x}, on the low binding energy side of the main NiO O1s intensity as well as a distinct deviation of the $Ni2p_{3/2}$ spectral features away from the typical NiO spectra. This can be explained by subtle changes of the charge densities around the vacancies which affect the oxidation states and bond lengths between surrounding Ni and O atoms as revealed by DFT calculations. These changes also affect the DOS near E_F as evidenced by experimentally obtained VB spectra. Calculated DOS near E_F suggest that changing Ni3d partial DOS are responsible for the deviation away from of the typical NiO shape. This is confirmed by similar changes observed at the XAS Ni L_3-edge as well as a distinct broadening of the lowest energy peak in the O K-edge spectra, which can be attributed to oxygen vacancies as evidenced by DFT calculations. Remarkably, at low temperatures when oxygen vacancies are almost fully replenished, the $Ni2p_{3/2}$ and Ni and O XAS spectra fully revert to their original shape even when residual oxygen vacancies can still be detected in the O1s spectra. This highlights that for NiO the O1s region is the most suitable to monitor changes of the chemical environment. This finding is further emphasized by the presence of a second, previously undetected O1s feature at 530 eV which suggests that oxygen vacancies may instigate the dissociation of water and mediate OH-bond formation, in particular to NiOOH, by way of chemisorption of OH and subsequent cooling. Since the formation of NiOOH is an important part of the OER in electrochemistry, the results presented here may help to improve the understanding of the basic mechanisms underlying the OER under in operando conditions. We will address the interaction of oxygen vacancies on NiO_x with water vapour in detail in another study.

Experimental Section

Sample Preparation

As starting point, polished standard (111)-orientated phosphor doped n-type silicon wafers with a resistivity of 0.5 Ω/cm and a size of 10 mm by 10 mm were used. The substrates were cleaned and etched with buffered HF and NH_4F solutions resulting in an ultra-flat and hydrogen terminated Si surface.[50,51] Afterwards, a 50 nm thick nickel film was deposited on the n-Si(111):H substrate using a sputter coater (Cressington 208HR; Ni sputter target by Kurt J. Lesker, 99.99% purity) which is operated under Ar atmosphere at room temperature (RT). The NiO_x films were prepared by step-wise thermal oxidation up to 270 °C heated by an external infrared laser (Limo, 808 nm wavelength; cw-mode) at an oxygen partial pressure of 0.5 mbar O_2 (Westfalen, purity 6.0) for different durations on stream (film Figure 1: oxidation at 250 °C for 39 min; film Figures 4–7: oxidation at 250 °C for 23 min/total oxygen exposure 326 min; film Figures 2 and 3: oxidation at 270 °C for 46 min/total oxygen exposure 200 min). The sample temperature was measured at the surface using a K-type thermocouple. Details are given in the Supporting Information. Following the same procedure heating-cooling cycles in oxygen were performed. Gas flows of O_2 were adjusted by mass flow controllers (Bronkhorst GmbH) in combination with a differential pumping stage regulating the final pressure in the analysis chamber.

Sample Characterization

In situ experiments in O_2 were performed at the BelChem beamline (UE56-2/PGM-1) located at the synchrotron radiation facility BESSY II (Berlin) in a dedicated NAP-XPS analysis system based on a SPECS Phoibos 150 analyzer. The UHV system is described in detail elsewhere.[52,53] All XPS spectra were recorded in normal photoemission geometry with a probing area of ≈150 μm×80 μm corresponding to the profile of the incident x-ray beam. The overall spectral resolution of the NAP-XPS analyzer is about 0.2 eV at 10 eV pass energy which was always used. The BE was calibrated using the valence band onset of metallic Ni with a pronounced Fermi edge with an accuracy of around 0.05 eV (see SI for details). In order to get an overview of the sample, survey spectra were recorded using $h\nu = 1020$ eV photon energy. The Ni2p core levels were measured with $h\nu = 1000$ eV only, while the O1s core levels were recorded with excitation energies of 680 and 1000 eV to allow depth profiling. The C1s region was screened with photon energies of 440 eV and 880 eV. Details on the XPS fit analysis and the quantification based on XPS are given in the Supporting Information.

The evolution of the WF during oxidation of the metallic Ni film to NiO and during subsequent heating-cooling cycles in O_2 was determined by additional recording of the secondary electron cut-off which allows determining the WF similar to UPS.

In parallel to XPS, XAS spectra were recorded. Therefore, the analyzer was adjusted to measure the auger electron yield at fixed kinetic energy of $E_{kin} = 300$ eV for the O K-edge and $E_{kin} = 500$ eV for the Ni L-edge while the excitation energy was steadily varied in 0.05 eV steps with a dwell time of 0.1 s. The energy range for the O K-edge was 520 eV to 560 eV whereas for the Ni–L edge 840 eV to 880 eV was chosen. So far, the evaluation of the XAS spectra was only done on a qualitative basis (fingerprint method). For a better comparison, a linear background was subtracted.

SEM micrographs were taken using a high-resolution ZEISS field emission-based microscope (LEO Gemini; SI only). The maximum lateral resolution is estimated to be in the range of about 10 nm depending on the structure and morphology of the thin film.

DFT Calculations

Density functional theory (DFT) calculations were performed based on the full-potential linearized augmented planewave (FLAPW) method using the Wien2k code.[54] Using the PBE functional, by minimizing the total energy of the cubic crystal of NiO (space group Fm-3 m) to the volume the theoretical lattice constant ($a = 4.166$ Å) was determined from the experimental lattice constant.[55,56] 500 k-points in the Brillouin zone (BZ), $G_{max} = 14$ $(a.u.)^{-1}$ (norm of the largest vector in the charge density Fourier expansion) and $R_{MT} \times k_{max} = 8.5$ were used in the calculation where R_{MT} and k_{max} are

the minimum muffin-tin radius and the maximum k-vector in the plane-wave expansion of the wave function, respectively. The calculations of DOS and XAS were performed using the TB-mBJ exchange-correlation potential with 50 k-points in the BZ on a relaxed 2×2×2 supercell containing of 32 Ni and 32 O atoms ($Ni_{RMT}=1.86$, $O_{RMT}=1.60$) with an antiferromagnetic spin configuration on alternating (111) planes (type-II antiferromagnetism) with the values of $G_{max}=14$ (a.u.)$^{-1}$ and $R_{MT}\times k_{max}=8.5$.[57]

Supporting Information

The authors have cited additional references within the Supporting Information.[58–71]

Acknowledgements

Financial support through the project "fundamentals of electrochemical phase boundaries at semiconductor/electrolyte interfaces" GEP-HE funded by the German Federal Ministry of Education and Research BMBF under contract 13XP5023A and by the European Union under the a-leaf project (732840-A-LEAF) as well as through the "Prometh$_2$eus" project funded by the BMBF under contract FKZ 03HY105E is gratefully acknowledged. We thank HZB for the allocation of synchrotron radiation beamtime at the BESSY II UE56_2-PGM-1 beamline and for financial support. We thank Wiebke Frandsen and Travis Jones for their support. Open Access funding enabled and organized by Projekt DEAL.

Conflict of Interests

The authors declare no conflict of interest.

Data Availability Statement

The data that support the findings of this study are available from the corresponding author upon reasonable request.

Keywords: adsorption · nickel · oxide · oxygen · vacancy

[1] P. T. Babar, A. C. Lokhande, M. G. Gang, B. S. Pawar, S. M. Pawar, J. H. Kim, *J. Ind. Eng. Chem.* **2018**, *60*, 493–497.
[2] V. V. Kaichev, A. A. Saraev, A. Yu. Gladky, I. P. Porosvirin, R. Blume, D. Teschner, M. Hävecker, A. Knop-Gericke, R. Schlögl, V. I. Bukhtiyarov, *Phys. Rev. Lett.* **2017**, *119*, 026001.
[3] E. A. Lashina, V. V. Kaichev, A. A. Saraev, Z. S. Vinokurov, N. A. Chumakova, G. A. Chumakov, V. I. Bukhtiyarov, *J. Phys. Chem. C* **2017**, 6874–6886.
[4] O. Guiader, P. Bernard, *J. Electrochem. Soc.* **2018**, *165*, A396–A406.
[5] R. P. Furstenau, G. McDougall, M. A. Langell, *Surf. Sci.* **1985**, *150*, 55–79.
[6] R. Poulain, A. Klein, J. Proost, *J. Phys. Chem. C* **2018**, *122*, 22252–22263.
[7] J. M. McKay, V. E. Henrich, *Phys. Rev. B* **1985**, *32(10)*, 6764–6772.
[8] D. Cappus, C. Xu, D. Ehrlich, B. Dillmann, C. A. Ventrice Jr., K. Al Shamery, H. Kuhlenbeck, H.-J. Freund, *Chem. Phys.* **1993**, *177*, 533–546.
[9] J. C. De Jesus, J. Carrazza, P. Pereira, F. Zaera, *Surf. Sci.* **1998**, *397*, 34–47.
[10] W.-L. Jang, Y.-M. Ming, W.-S. Hwang, *Vacuum* **2009**, *83*, 596–598.
[11] T. Zhang, M.-Y. Wu, D.-Y. Yan, J. Mao, H. Liu, W.-B. Hu, X.-W. Du, T. Ling, S.-Z. Qiao, *Nano Energy* **2018**, *43*, 103–109.
[12] J.-Y. Jung, J.-Y. Yu, S. Yoon, B. Yoo, J.-H. Lee, *Adv. Sustainable Syst.* **2018**, *2*, 1800083.
[13] N. Weidler, J. Schuch, F. Knaus, P. Stenner, S. Hoch, A. Maljusch, R. Schäfer, B. Kaiser, W. Jaegermann, *J. Phys. Chem. C* **2017**, *121*, 6455–6463.
[14] M. Fingerle, S. Tengeler, W. Calvet, W. Jaegermann, T. Mayer, *J. Electrochem. Soc.* **2020**, *167*, 136514.
[15] V. Patil, S. Pawar, M. Chougule, P. Godse, R. Ratnakar, S. Sen, P. Joshi, *J. Surf. Eng. Mater. Adv. Technol.* **2011**, *1*, 35–41.
[16] M. S. Jamal, S. A. Shahahmadi, P. Chelvanathan, H. F. Alharbi, M. R. Karim, M. A. Dar, M. Luqman, N. H. Alharthi, Y. S. Al-Harthi, M. Aminuzzaman, N. Asim, K. Sopian, S. K. Tiong, N. Amin, Md. Akhtaruzzaman, *Results Phys.* **2019**, *14*, 102360.
[17] Z. Luo, L. Liu, X. Yang, X. Luo, P. Bi, Z. Fu, A. Pang, W. Li, Y. Yi, *ACS Appl. Mater. Interfaces* **2020**, *12*, 39098–39107.
[18] H. Kuhlenbeck, G. Odörfer, R. Jaeger, G. Illing, M. Menges, Th. Mull, H.-J. Freund, *Phys. Rev. B* **1991**, *43*, 1969–1986.
[19] P. Sahoo, D. K. Misra, J. Salvador, J. P. A. Makongo, G. S. Chaubey, N. J. Takas, J. B. Wiley, P. F. P. Poudeu, *J. Solid State Chem.* **2012**, *190*, 29–35.
[20] M. Napari, T. N. Huq, R. L. Z. Hoye, J. L. MacManus-Driscoll, *InfoMat.* **2020**, *3*, 1–41.
[21] M. Fingerle, S. Tengeler, W. Calvet, T. Mayer, W. Jaegermann, *J. Electrochem. Soc.* **2018**, *165*, H3148–H3153.
[22] N. D. Hoa, P. V. Tong, C. M. Hung, N. V. Duy, N. V. Hieu, *Int. J. Hydrogen Energy* **2018**, *43(19)*, 9446–9453.
[23] N. Kitakatsu, V. Maurice, C. Hinnen, P. Marcus, *Surf. Sci.* **1998**, *407*, 36–58.
[24] F. Ullrich, S. Hillebrandt, S. Hietzschold, V. Rohnacher, T. Marszalek, W. Kowalsky, R. Lovrincic, S. Beck, E. Mankel, A. Pucci, *ACS Appl. Energ. Mater.* **2018**, *1*, 3113–3122.
[25] A. F. Carley, S. D. Jackson, J. N. O'Shea, M. W. Roberts, *Surf. Sci.* **1999**, *440*, L868–L874.
[26] M. A. van Veenendaal, G. A. Sawatzky, *Phys. Rev. Lett.* **1993**, *70*, 2459–2462.
[27] L. Sangaletti, L. E. Depero, F. Parmigiani, *Solid State Commun.* **1997**, *103(7)*, 421–424.
[28] Y. S. Chen, J. F. Kang, B. Chen, B. Gao, L. F. Liu, X. Y. Liu, Y. Y. Wang, L. Wu, H. Y. Yu, J. Y. Wang, Q, Chen, E. G. Wang, *J. Phys. D* **2012**, *45*, 065303.
[29] I. Preda, R. J. O. Mossanek, M. Abbate, L. Alvarez, J. Mendez, A. Gutierrez, L. Soriano, *Surf. Sci.* **2012**, *606*, 1426–1430.
[30] L. Soriano, I. Preda, A. Gutierrez, S. Palacin, M. Abbate, A. Vollmer, *Phys. Rev. B* **2007**, *75*, 233417.
[31] S. Uhlenbrock, C. Scharfschwerdt, M. Neumann, G. Illing, H–J. Freund, *J. Phys. Condens. Matter* **1992**, *4*, 7973–7978.
[32] R. J. O. Mossanek, I. Preda, M. Abbate, J. Rubio-Zuazo, G. R. Castro, A. Vollmer, A. Gutierrez, *Chem. Phys. Lett.* **2011**, *501*, 437–441.
[33] M. C. Biesinger, B. P. Payne, A. P. Grosvenor, L. W. M. Lau, A. R. Gerson, R. St. C. Smart, *Appl. Surf. Sci.* **2011**, *257*, 2717–2730.
[34] A. P. Grosvenor, M. C. Biesinger, R. St. C. Smart, N. S. McIntyre, *Surf. Sci.* **2006**, *600*, 1771–1779.
[35] I. Preda, M. Abbate, A. Gutierrez, S. Palacin, A. Vollmer, L. Soriano, *J. Electron Spectrosc. Relat. Phenom.* **2007**, *156–158*, 111–114.
[36] L. Soriano, A. Gutierrez, I. Preda, S. Palacin, J. M. Sanz, M. Abbate, J. F. Trigo, A. Vollmer, P. R. Bressler, *Phys. Rev. B* **2006**, *74*, 193402.
[37] F. M. F. De Groot, J. C. Fuggle, B. T. Thole, G. A. Sawatzky, *Phys. Rev. B* **1990**, *42(9)*, 5459–5468.
[38] G. Van der Laan, *J. Magn. Magn. Mater.* **1999**, *192*, 297–304.
[39] L. Soriano, M. Abbate, J. Vogel, J. C. Fuggle, A. Fernandez, A. R. Gonzalez-Elipe, M. Sacchi, *Chem. Phys. Lett.* **1993**, *208(6)*, 460–464.
[40] S. Chakrabarti, D. Carolan, B. Alessi, P. Maguire, V. Svecek, D. Mariotti, *Nanoscale Adv.* **2019**, *1*, 4915–4925.
[41] F. Rieck, J. Koch, G. Lilienkamp, F. Körkemeyer, H. J. Maier, J. Caro, K. Lange, *Int. J. Electrochem.* **2018**, Article ID 9875438.
[42] Z. Lin, C. Du, B. Yan, C. Wang, G. Yang, *Nat. Commun.* **2018**, *9*, 4036.
[43] P. A. Thiel, T. E. Madey, *Surf. Sci. Rep.* **1987**, *7*, 211–385.
[44] D. J. Simpson, T. Bredow, A. R. Gerson, *Theor. Chem. Acc.* **2005**, *114*, 242–252.
[45] M. T. Greiner, M. G. Helander, Z.-B. Wang, W.-M. Tang, Z.-H. Lu, *J. Phys. Chem. C* **2010**, *114*, 19777–19781.
[46] T. Dutta, P. Gupta, A. Gupta, J. Narayan, *J. Phys. D* **2010**, *43*, 105301.
[47] J. Y. Zhang, W. W. Li, R. L. Z. Hoye, J. L. MacManus-Driscoll, M. Budde, O. Bierwagen, L. Wang, Y. Du, M. J. Wahila, L. F. J. Piper, T.-L. Lee, H. J. Edwards, V. R. Dhanak, K. H. L. Zhang, *J. Mater. Chem. C* **2018**, *6*, 2275–2282.

[48] R. Poulain, G. Lumbeek, J. Hunka, J. Proost, H. Savolainen, H. Idrissi, D. Schryvers, N. Gauquelin, A. Klein, *ACS Appl. Electron. Mater.* **2022**, *4*, 2718–2728.
[49] K. X. Steirer, P. F. Ndione, N. E. Widjonarko, M. T. Lloyd, J. Meyer, E. L. Ratcliff, A. Kahn, N. R. Armstrong, C. J. Curtis, D. S. Ginley, J. J. Berry, D. C. Olson, *Adv. Energy Mater.* **2011**, *1*, 813–820.
[50] H. Angermann, W. Henrion, A. Röseler, M. Rebien, *Mat. Sci. Eng.* **2000**, *B73*, 178–183.
[51] G. S. Higashi, Y. J. Chabal, G. W. Trucks, K. Raghavachari, *Appl. Phys. Lett.* **1990**, *56*, 656.
[52] H. Bluhm, M. Hävecker, A. Knop-Gericke, E. Kleimenov, R. Schlögl, D. Teschner, V. I. Bukhtiyarov, D. F. Ogletree, M. Salmeron, *J. Phys. Chem. B* **2004**, *108*, 14340–14347.
[53] A. Knop-Gericke, E. Kleimenov, M. Hävecker, R. Blume, D. Teschner, S. Zafeiratos, R. Schlögl, V. I. Bukhtiyarov, V. V. Kaichev, I. P. Prosvirin, A. I. Nizovskii, H. Bluhm, A. Barinov, P. Dudin, M. Kiskinova, *Adv. Catal.* **2009**, *52*, 213–272.
[54] P. Blaha, K. Schwarz, P. Sorantin, S. B. Trickey, *Comput. Phys. Commun.* **1990**, *59(2)*, 399–415.
[55] J. P. Perdew, K. Burke, M. Ernzerhof, *Phys. Rev. Lett.* **1996**, *77*, 3865–3868.
[56] S. Sasaki, K. Fujino, Y. Takeuchi, *Proc. Jpn. Acad. Ser. B* **1979**, *55(2)*, 43–48.
[57] F. Tran, P. Blaha, *Phys. Rev. Lett.* **2009**, *102*, 226401.
[58] D. A. Shirley, *Phys. Rev. B* **1972**, *5*, 4709–4714.
[59] S. Doniach, M. Sunjic, *J. Phys. C* **1970**, *3*, 285–291.
[60] J. J. Yeh, I. Lindau, *At. Data Nucl. Data Tables* **1985**, *32*, 1–155.
[61] M. P. Seah, *Surf. Interface Anal.* **1986**, *9*, 85–98.
[62] B. Frank, R. Blume, A. Rinaldi, A. Trunschke, R. Schlögl, *Angew. Chem. Int. Ed.* **2011**, *50*, 10226–10230.
[63] S. Reiche, R. Blume, X. C. Zhao, D. Su, E. Kunkes, M. Behrens, R. Schlögl, *Carbon* **2014**, *77*, 175–183.
[64] R. S. Weatherup, C. Baehtz, B. Dlubak, B. C. Bayer, P. R. Kidambi, R. Blume, R. Schlögl, S. Hofmann, *Nano Lett.* **2013**, *13*, 4624–4631.
[65] R. S. Weatherup, B. C. Bayer, R. Blume, C. Baehtz, P. R. Kidambi, M. Fouquet, C. T. Wirth, R. Schlögl, S. Hofmann, *ChemPhysChem* **2012**, *13*, 2544–2549.
[66] M. Sterrer, H.-J. Freund, in *Surface and Interface Science*, Vol. 3 (Ed.: K. Wandelt), Wiley-VCH, Weinheim, **2013**, pp. 229–278.
[67] M. A. Langell and M. H. Nassir, *J. Phys. Chem.* **1995**. *99*, 4162–4169.
[68] M. A. Munoz-Marquez, R. E. Tanner, D. P. Woodruff, *Surf. Sci.* **2004**, *565*, 1–13.
[69] L. Liu, S. Wang, S. Liu, Q. Guo, J. Guo, *Surf. Sci.* **2018**, *667*, 8–12.
[70] M. Hävecker, M. Cavalleri, R. Herbert, R. Follath, A. Knop-Gericke, C. Hess, K. Hermann, R. Schlögl, *Phys. Status Solidi B* **2009**, *246*, 1459–1469.
[71] R. Smoluchowski, *Phys. Rev.* **1941**, *60*, 661–674.

Manuscript received: March 29, 2023
Revised manuscript received: September 8, 2023
Accepted manuscript online: September 14, 2023
Version of record online: September 27, 2023